Supplymentary Information

Four-phonon scattering and multi-valley characters induce high thermoelectric performance in TlAgSe: A first-principles investigation

Zhaoying Wang[1*], Shaoshuai Guo[1], Yinsheng Li[1], Maixia Fu[1], Guangtao Wang[2], Zhenghao Hou[3,*]

[1]*Key Laboratory of Grain Information Processing and Control, Ministry of Education, College of Information Science and Engineering, Henan University of Technology, Zhengzhou, 450001, China*

[2] *College of Physics, Henan Normal University, Xinxiang 450007, China*

[3] *Shijiazhuang Key Laboratory of Low Carbon Energy Materials, College of Chemical Engineering, Shijiazhuang University, Shijiazhuang 050035, China*

** Corresponding author.*

E-mail addresses: wangzhaoying@haut.edu.cn; 2109004@sjzc.edu.cn

Computational details:

The energy cutoff for the plane-wave expansion was set to 450 eV. Both the lattice parameters and atomic coordination are fully relaxed until the convergency criteria of total energy < 10^{-8} eV and residual interatomic force < 10^{-4} eV Å^{-1}, respectively. The Brillouin zone was sampled by Monkhorst-Pack method with the *k*-point mesh 5 × 11 × 7. Considering the overestimated band gaps in PBE functional, the electronic band structure was computed using the Heyd-Scuseria-Ernzerhof (HSE06) hybrid functional[1, 2]. The LOBSTER code was utilized to evaluate the chemical bonding strength through the crystal orbital Hamiltonian population (COHP)[3]. The *ab initio* molecular dynamics (AIMD) simulations[4] were performed within the canonical ensemble using a Nose-Hoover thermostat (NVT) at 300 and 600 K with a time step of 1 fs and a total time 3 ps.

The ALAMODE code[5-7] was used to obtain the second- to fourth-order interatomic force constants (IFCs) within a 2 × 4 × 2 supercell and 3 × 3 × 3 Monkhorst-Pack *k*-mesh. The finite displacement method was utilized to extract the second order IFCs from 15 random displaced configurations. To capture the longitudinal optical and transverse optical phonon node splitting near the zone-center, which introduced by the long-range correction to the dynamic matrix, the Born effective charge was calculated through density functional perturbation theory (DFPT)[8]. The accurate third- and four-order IFCs were obtained from the machine learning techniques within the compressed sensing lattice dynamics (CSLD) method[9]. The training set of CLSD was obtained from the AIMD simulations, which is conducted at 300 K within the canonical ensemble using a Nose-Hoover thermostat (NVT) using a 2 × 4 × 2 supercell with a time step of 1 fs and a total time 3 ps. The cutoff interactions up to the 10th and 4th nearest neighbors were adopted in calculation of anharmonic third- and four-order IFCs, respectively. The self-consistent phonon (SCPH) mode computes temperature-dependent phonon frequencies[10, 11]. After the SCPH iteration converges, the anharmonic correction to the harmonic force constant can be obtained. After obtaining the second-, third-, and four-order IFCs, the thermal transport properties were calculated using ShengBTE

package[12, 13]. The convergence of thermal conductivity was tested with different *q*-mesh, as displayed in **Fig. S3(a)** of **Supporting Information**. The *q*-grid 13 × 26 × 13 was used in calculation. The scalebroad = 0.1 was adopted in all calculations.

The electrical transport properties were calculated through Onsager coefficients as implemented in *ab initio* scattering and transport (AMSET) code[14], which is widely used in both the two-dimensional and bulk thermoelectric materials[15, 16]. The carrier relaxation time was evaluated by considering three scattering mechanisms, including the elastic ionized impurity scattering (IMP), the elastic acoustic deformation potential scattering (ADP), and the inelastic polar optical phonon scattering (POP). The dielectric constants and polar-phonon frequency were calculated by using density functional perturbation theory (DFPT)[8]. The interpolation electronic eigenvalues were determined using a *k*-grid of 31 × 55 × 33. The related constants, including deformation potential, elastic constants, static and high frequency dielectric constants, and polar-phonon frequency are listed in **Table. S1**. The default values of defect-charge and compensation-factor were adopted.

The electrical transport properties were calculated through Onsager coefficients as implemented in *ab initio* scattering and transport (AMSET) code[14]. The spectral conductivity is calculated as:

$$\sum_{\alpha\beta}(\varepsilon) = \sum_{n} \frac{d\mathbf{k}}{8\pi^2} \upsilon_{n\mathbf{k},\alpha} \upsilon_{n\mathbf{k},\beta} \tau_{n\mathbf{k}} \delta(\varepsilon - \varepsilon_{n\mathbf{k}}) \tag{S1}$$

where α, β denote Cartesian coordinate, $\varepsilon_{n\mathbf{k}}$ and $\upsilon_{n\mathbf{k},\alpha}$ are energy and group velocity of band index n and wave vector $\mathbf{k}$, respectively. The moments of the generalized transport coefficients can be calculated based on the spectral conductivity:

$$L^{n}_{\alpha\beta} = e^2 \int \sum_{\alpha\beta}(\varepsilon)(\varepsilon - \varepsilon_F)^n \left[-\frac{\partial f^0}{\partial \varepsilon} \right] d\varepsilon \tag{S2}$$

where e is the electron charge and ε_F is the Fermi level at a certain doping concentration and temperature T. The Fermi-Dirac distribution is given by

$$f^0_{n\mathbf{k}} = \frac{1}{\exp\left[(\varepsilon_{n\mathbf{k}} - \varepsilon_F)/k_B T\right] + 1} \tag{S3}$$

where k_B is the Boltzmann constant. Electrical conductivity (σ), Seebeck coefficient (S), and the charge carrier contribution to thermal conductivity (κ) are obtained as:

$$\sigma_{\alpha\beta} = L^n_{\alpha\beta} \tag{S4}$$

$$S_{\alpha\beta} = \frac{1}{eT}\frac{L^1_{\alpha\beta}}{L^0_{\alpha\beta}} \tag{S5}$$

$$\kappa_{\alpha\beta} = \frac{1}{e^2T}\left[\frac{(L^1_{\alpha\beta})^2}{L^0_{\alpha\beta}} - L^2_{\alpha\beta}\right] \tag{S6}$$

The carrier relaxation time was evaluated by considering three scattering mechanisms, including the elastic ionized impurity scattering (IMP), the elastic acoustic deformation potential scattering (ADP), and the inelastic polar optical phonon scattering (POP).

The elastic scattering rate can be described as:

$$\tau^{-1}_{n\mathbf{k}} = \sum_m \int \frac{2\pi d^3q}{\hbar\Omega}\left|g_{nm}(\mathbf{k},\mathbf{q})\right|^2\left[1-\frac{v_{n\mathbf{k}}v_{m\mathbf{k}+\mathbf{q}}}{\left|v_{n\mathbf{k}}\right|^2}\right]\delta(\varepsilon_{n\mathbf{k}}-\varepsilon_{m\mathbf{k}+\mathbf{q}}) \tag{S7}$$

and the inelastic scattering rate was:

$$\tau^{-1}_{n\mathbf{k}} = \sum_m \int \frac{d^3q}{\Omega}\tau^{-1}_{n\mathbf{k}\to m\mathbf{k}+\mathbf{q}} \tag{S8}$$

$$\begin{aligned}\tau^{-1}_{nk\to mk+q} = \frac{2\pi}{\hbar}\left|g_{nm}(\mathbf{k},\mathbf{q})\right|^2 \times[&(n_{po}+1-f_{m\mathbf{k}+\mathbf{q}})\delta(\varepsilon_{n\mathbf{k}}-\varepsilon_{m\mathbf{k}+\mathbf{q}}-\hbar\omega_{po}) \\ &+(n_{po}-f_{m\mathbf{k}+\mathbf{q}})\delta(\varepsilon_{n\mathbf{k}}-\varepsilon_{m\mathbf{k}+\mathbf{q}}+\hbar\omega_{po})]\end{aligned} \tag{S9}$$

where $n\mathbf{k}$ represents the initial state of the n-th electron, and the n and $\mathbf{k}$ are the band index and electron wave vector, respectively. $m\boldsymbol{k}$ +$\mathbf{q}$ denotes the final state within the Born approximation when the electron initial state $n\mathbf{k}$ couples with the phonon at the wave vector $\mathbf{q}$ and frequency $\omega_{\mathbf{q}}$. The δ, n_{po}, and f mean the Dirac delta function, the Bose- Einstein distribution, and the Fermi-Dirac distribution, respectively. $\hbar\omega_{\mathbf{q}}$ and $+\hbar\omega_{\mathbf{q}}$ refer to the energy change by emitting (-) and absorbing (+) of a phonon. The g_{nm} represents the electron–phonon coupling matrix elements from certain scattering mechanisms, including g^{ADP}_{nm}, g^{IMP}_{nm}, and g^{POP}_{nm}. Based on a series of execution parameters, including wave function coefficient and band structure, elastic constant

tensor and deformation potential constant (required for g_{nm}^{ADP}), static and high frequency dielectric constant and polar optical phonon frequency (required for g_{nm}^{IMP}, and g_{nm}^{POP}), the reliable carrier relaxation time was obtained by using AMSET code.

Tables and Figures

Table S1 The parameters used in the electronic transport calculation with AMSET code.

AMSET parameters	TlAgSe
Deformation potential tensor (valence band maximum)	$\begin{pmatrix} 0.67 & 0.31 & 0.03 \\ 0.31 & 3.29 & 0.01 \\ 0.03 & 0.01 & 1.70 \end{pmatrix}$
Deformation potential tensor (conduction band minimum)	$\begin{pmatrix} 0.88 & 0.29 & 0.13 \\ 0.29 & 3.54 & 0.41 \\ 0.13 & 0.41 & 0.37 \end{pmatrix}$
Elastic constant tensor (GPa)	$\begin{pmatrix} 35.4 & 31.1 & 29.2 & 0 & 0 & 0 \\ 31.1 & 65.4 & 39.7 & 0 & 0 & 0 \\ 29.2 & 39.7 & 52.7 & 0 & 0 & 0 \\ 0 & 0 & 0 & 20.1 & 0 & 0 \\ 0 & 0 & 0 & 0 & 13.0 & 0 \\ 0 & 0 & 0 & 0 & 0 & 12.3 \end{pmatrix}$
High-requency dielectric constant tensor (ε_∞)	$\begin{pmatrix} 15.3 & 0 & 0 \\ 0 & 17.0 & 0 \\ 0 & 0 & 14.5 \end{pmatrix}$
Static dielectric constant tensor (ε_0)	$\begin{pmatrix} 64.1 & 0 & 0 \\ 0 & 46.6 & 0 \\ 0 & 0 & 40.5 \end{pmatrix}$
Polar optical phonon frequency (THz)	2.06

Table S2 Anisotropic and average effective mass (unit: m_e) of VBM and CBM.

	m_x	m_y	m_z	m_b
VBM	0.51	0.14	0.72	0.37
CBM	0.25	0.38	0.38	0.33

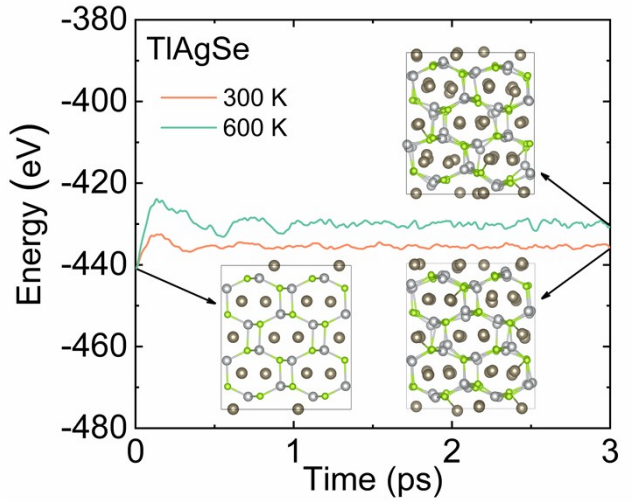

Fig. S1 The AIMD simulated total energy of TlAgSe as function of time-step at 300 K and 600 K. The inerted configuration at left pannel is initio structure, while the right pannel refer to the finanl structures to 300 K (down) and 600 K (up), respectively.

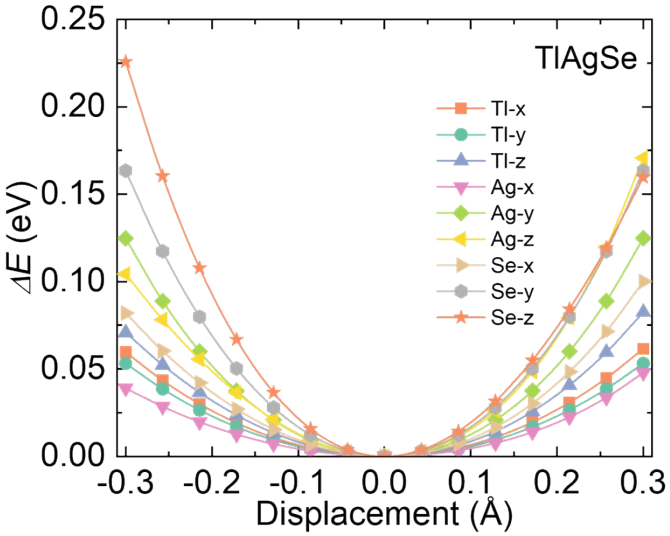

Fig. S2 Anisotropic potential energy as function of displacement for irreducible atoms in TlAgSe.

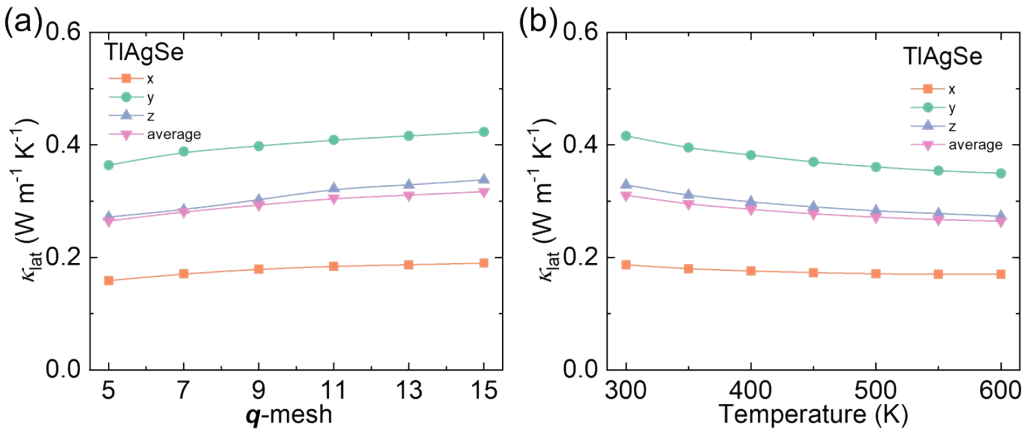

Fig. S3 (a) Convergence test of anisotropic lattice thermal conductivity for TlAgSe with different q-mesh ($q \times 2q \times q$) at 300 K. (b) The anisotropic lattice thermal conductivity for TlAgSe as function of temperature.

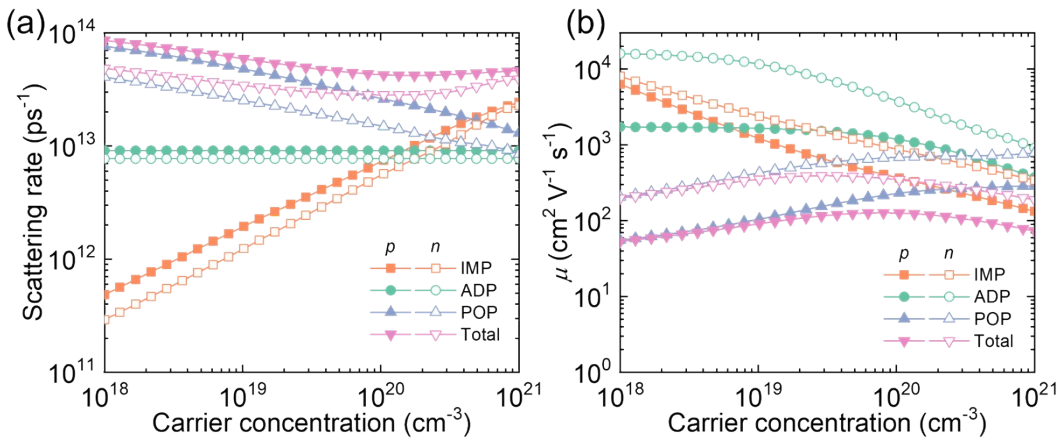

Fig. S4 The calculated (a) scattering rates and (b) carrier mobility as function of carrier concentration under various scattering mechanisms for *p*-type and *n*-type doping, respectively.

References

1. A. V. Krukau, O. A. Vydrov, A. F. Izmaylov and G. E. Scuseria, *J. Chem. Phys.*, 2006, **125**, 224106.
2. J. Paier, R. Hirschl, M. Marsman and G. Kresse, *J. Chem. Phys.*, 2005, **122**, 234102.
3. V. L. Deringer, A. L. Tchougreeff and R. Dronskowski, *J. Phys. Chem. A*, 2011, **115**, 5461-5466.
4. M. E. Tuckerman, P. J. Ungar, T. von Rosenvinge and M. L. Klein, *J. Phys. Chem*, 1996, **100**, 12878-12887.
5. T. Tadano, Y. Gohda and S. Tsuneyuki, *J. Phys.: Condens. Matter*, 2014, **26**, 225402.
6. T. Tadano and S. Tsuneyuki, *Phys. Rev. B*, 2015, **92**, 054301.
7. Y. Oba, T. Tadano, R. Akashi and S. Tsuneyuki, *Phys. Rev. Mater.*, 2019, **3**, 033601.
8. S. Baroni, S. de Gironcoli, A. Dal Corso and P. Giannozzi, *Rev. Mod. Phys.*, 2001, **73**, 515-562.
9. F. Zhou, B. Sadigh, D. Åberg, Y. Xia and V. Ozoliņš, *Phys. Rev. B*, 2019, **100**, 184309.
10. N. R. Werthamer, *Phys. Rev. B*, 1970, **1**, 572-581.
11. T. Tadano and S. Tsuneyuki, *Phys. Rev. Lett.*, 2018, **120**, 105901.
12. W. Li, J. Carrete, N. A. Katcho and N. Mingo, *Comput. Phys. Commun.*, 2014, **185**, 1747-1758.
13. Z. Han, X. Yang, W. Li, T. Feng and X. Ruan, *Comput. Phys. Commun.*, 2022, **270**, 108179.
14. A. M. Ganose, J. Park, A. Faghaninia, R. Woods-Robinson, K. A. Persson and A. Jain, *Nat. Commun.*, 2021, **12**, 2222.
15. T. C. Yue, Y. C. Zhao, J. Ni, S. Meng and Z. H. Dai, *npj Comput. Mater.*, 2023, **9**, 17.
16. S. Bai, M. Wu, J. Zhang, D. Luo, D. Wan, X. Li and S. Tang, *Chem. Eng. J.*, 2023, **455**, 140832.